Inhomogeneous strain relaxation in triple-barrier *p*-Si/SiGe nanostructures

C. D. Akyüz
Department of Physics, Brown University, Providence, Rhode Island 02912

H. T. Johnson, A. Zaslavsky, and L. B. Freund
Division of Engineering, Brown University, Providence, Rhode Island 02912

D. A. Syphers
Physics Department, Bowdoin College, Brunswick, Maine 04011

(Received 11 December 1998; revised manuscript received 4 June 1999)

Resonant tunneling measurements are used to probe size-induced strain relaxation in *p*-Si/SiGe triple-barrier nanostructures with a narrow (~10 Å) middle barrier, where the confined subbands depend strongly on the strain and bias-dependent coupling between the two neighboring quantum wells. In structures with $2.0 \geqslant D \geqslant 0.25\ \mu\text{m}$ diameter, shifts in the strain-dependent subband energies are clearly observable in the tunneling current. Further, in the smallest structures ($D \leqslant 0.17\ \mu\text{m}$), tunneling through discrete states confined by inhomogeneous-strain-induced lateral potentials dominates the $I(V)$. Magnetotunneling measurements on a $D=0.17\ \mu\text{m}$ structure reveal a ~75-Å effective length of the strain-induced lateral confinement potential. Based on our previous measurements of double-barrier nanostructures and the finite element calculations of the strain distribution in these triple-barrier structures, we conclude that the $I(V)$ peak shifts in larger devices are due to uniform strain relaxation, whereas in smaller devices the fine structure in the $I(V)$ is due to coupled inhomogeneous-strain-induced discrete quantum-dot or ring states in neighboring wells.
[S0163-1829(99)14347-9]

Quantum structures, like quantum wells, wires, and dots in which carriers are confined to fewer than three dimensions, are essential to the study of single or interacting carriers in quantum environments. Heterojunction band discontinuities, like at the $GaAs/Al_xGa_{1-x}As$ junctions, are commonly used to create two-dimensional (2D) electron gases which are often used for fabricating lower-dimensional quantum structures with other confinement techniques, like etching or electrostatic gating. The successful epitaxy of strained heterostructures, like Si/SiGe, with uniform biaxial strain and minimal defects in the lattice structure has led to a number of experimental and theoretical studies on strain and its influence on the electronic properties of semiconductors.[1–3] Strain-induced confinement potentials provide a relatively new tool for fabricating reduced dimensionality structures.

The properties of homogeneous biaxial strain arising from lattice mismatch and its effects on the electronic properties of semiconductor thin films are well understood.[2,4,5] In a pseudomorphically grown heterostructure of lattice-mismatched materials, the lattice in the strained layers is under biaxial compression. Biaxial compression can be linearly decomposed into a hydrostatic compression and a uniaxial expansion. In semiconductors with zinc-blende symmetry, the hydrostatic compression changes the band gap but shifts the valence bands uniformly, leaving unchanged the heavy-hole (HH) and light-hole (LH) band-edge degeneracy. The uniaxial expansion introduces an interaction between the bands, lifting the HH-LH band-edge degeneracy and increasing the anisotropy and nonparabolicity of the hole dispersions. A precise control over strain distribution in semiconductor devices can be used to fabricate interesting quantum structures. Previously, strain has been utilized to fabricate quantum wires or dots by stressor patterning,[6] or epitaxial overgrowth.[7,8] Recently, it has been discovered that relaxation of the strained layers at the free surface of etched nanostructures has a significant influence on their electronic properties.[9–13] Lateral displacement of the free surface relaxes the strained layers and leads to an inhomogeneous strain distribution throughout the structure. The effects of size-induced strain relaxation on the electronic properties of p-$Si/Si_{0.25}Ge_{0.75}$ double-barrier resonant tunneling (RT) diodes with ~1% lattice mismatch are observable in devices with lateral dimensions as large as 0.75 μm; the inhomogeneity in the strain distribution becomes dominant when the lateral size falls below 0.3 μm.[14] Nonuniform strain induces a lateral confinement potential in nanostructures, and enables experimental realization of quantum states such as quantum wires, dots, or ring states.[10–13]

We have measured the influence of size-induced strain relaxation on the electronic properties of strained Si/SiGe triple-barrier RT structures with strong interwell coupling. The effects of strain relaxation in double-barrier Si/SiGe nanostructures have been reported earlier.[9,11,12,14] In triple-barrier RT structures with a narrow middle barrier (~10 Å), the 2D subband energies of the active region depend strongly on the coupling between the two quantum wells.[15] The interwell coupling is sensitive to the strain which affects the coupling strength and the energy levels of the 2D subbands in the individual quantum wells. In triple-barrier submicron structures with a thin middle barrier, as the strained well layers expand outwards at the perimeter, the middle barrier is under tensile strain. The thicker outer barriers of double- and triple-barrier submicron structures are strained in a similar

 ©1999 The American Physical Society

fashion; however, the corresponding effect is much smaller. Hence our RT measurements of Si/SiGe triple-barrier submicron structures probe the size-induced tensile strain in the Si middle barrier together with the strain relaxation in the SiGe well and emitter layers. In $T=1.7$ K $I(V)$ data of RT devices with effective diameters in the range of $2.0 \geqslant D \geqslant 0.17$ μm, we have observed shifts in the RT peaks due to uniform strain relaxation. In smaller structures ($D \leqslant 0.17$ μm) the additional fine structure in the RT current due to the inhomogeneous-strain-induced lateral confinement dominates the $I(V)$ characteristics. The effects of lateral quantization are observable even in larger structures with $D=0.29$ μm. To analyze our data we have calculated the effects of uniform strain relaxation on the position of RT $I(V)$ peaks. We have employed additional magnetotunneling measurements to estimate the effective length of the inhomogeneous-strain-induced confinement potential.

Deep-submicron triple-barrier RT structures were fabricated from strained p-Si/Si$_{0.8}$Ge$_{0.2}$ asymmetric triple-barrier RT material. The details of the structural design were published previously.[15] The undoped active regions consist of two Si$_{0.8}$Ge$_{0.2}$ wells of widths $W_1 \sim 35$ Å and $W_2 \sim 28$ Å separated by a narrow Si middle barrier of width $L \sim 10$ Å and confined by ~45-Å outer Si barriers. The active region is sandwiched in turn by doped p-Si/Si$_{0.8}$Ge$_{0.2}$ emitter and collector reservoirs. The processing involved the etching of a mesa of nominal diameter, followed by planarization and contact pad deposition.[9] According to the scanning electron microscope observations, the effective diameters D of the structures are within 500 Å of the nominal lateral sizes of their etch-mask pads due to the etch undercut. Surface depletion due to surface states, including states induced by plasma etching defects, requires careful consideration in deep submicron structures. While our previous measurements on double-barrier structures exhibited good scaling of current with device area, and hence ruled out a large damaged region depleted of carriers,[9] a very small (<100 Å) surface depletion region cannot be excluded. Such surface depletion would affect the interpretation of the fine structure in the $I(V)$ data on the smallest ($D<0.15$ μm) devices, where the strain-induced lateral potentials near the surface become important. However, the consistent evolution of the $I(V)$ from larger devices, where surface depletion is irrelevant, to the smallest ones, [9,12–14] together with our magnetotunneling measurements described below, argue against significant surface depletion. Therefore, in our analysis we will assume carrier depletion at the etched (and oxide passivated) surfaces to be negligible.

Tunneling current transport through triple-barrier structures can be analyzed analogously to the well-known double-barrier case. When a bias V is applied to the top contact, a tunneling current flows through the quantized 2D hole subbands in the active region, subject to the usual energy E and in-plane momentum $\mathbf{k}_\perp$ conservation rules.[16] Self-consistent potential distribution calculations have been successfully employed to convert the voltages at which peaks are observed to alignments of confined subband energy levels with respect to the occupied emitter states,[17,18] providing an experimental probe of the subband energies.

In large devices with uniform strain, the 2D subbands confined in the active region can be treated as coupled states of the HH and LH subbands of the neighboring quantum wells. Figure 1 shows the results of self-consistent calculations of the potential profiles of a large, fully strained triple-barrier structure at $V=0$, 275, and 500 mV together with the energy levels of the 2D subbands in the individual wells corresponding to a double-barrier potential and of the coupled 2D subbands of the triple-barrier structure. Since the strength of the inter-well coupling depends on the applied bias,[15] the in-plane dispersions of the subbands in the active region of triple-barrier RT structures are more sensitive to the applied bias than the double-barrier devices. The characteristic $I(V)$ at $T=1.7$ K of a large $D=2.0$ μm device, where the effects of strain relaxation are negligible, is shown in Fig. 2. The resonant peak at $V \sim 500$ mV corresponds to a tunneling from the emitter to the LH subband in the first well [Fig. 1(c)], and then directly to the collector, with a transport mechanism reduced to the previously studied double-barrier case.[12] Hence, we restrict our analysis to the lower bias range: $V \leqslant 400$ mV, where the interwell coupling plays a significant role. However, we have used the maximum current density in the LH peak of the 2.0-μm device in Fig. 2 to more accurately calibrate the effective diameters of the smaller devices because of its high peak-to-valley ratio and relative insensitivity to the inhomogeneous-strain-induced confinement potential.[12] It is important to reiterate that the effective diameters are within 500 Å of the nominal sizes of the etch masks.

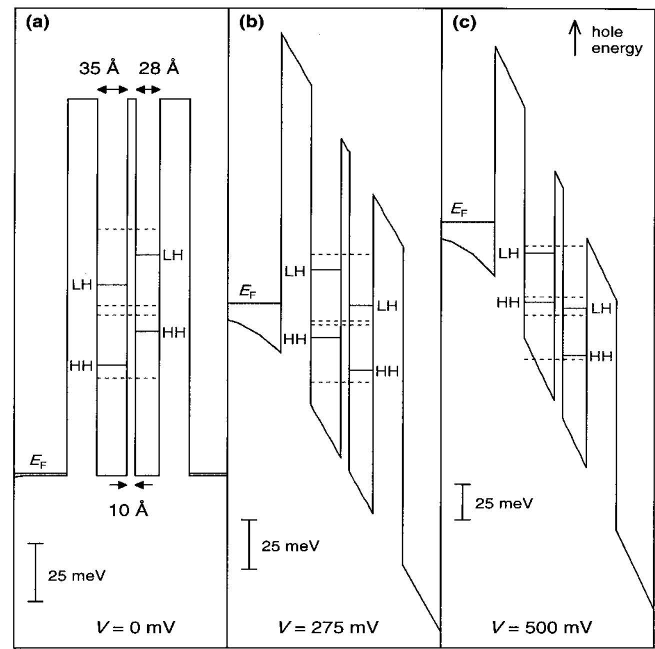

FIG. 1. The self-consistent potential profiles of a fully strained p-Si/Si$_{0.8}$Ge$_{0.2}$ triple-barrier structure at $V=0$ (a), 275 (b), and 500 (c) mV. The vertical axes correspond to the hole energy. The different energy scales (indicated by 25-meV vertical markers) are used for a clearer presentation of the energy levels. The solid lines in the individual quantum wells are the energy levels of the 2D subbands of a corresponding double-barrier potential. The dashed lines mark the energy levels of the coupled 2D subbands in the triple-barrier potential (6×6 Luttinger-Kohn Hamiltonian calculations).

The three low-bias peaks of a $D=2.0$ μm device shown

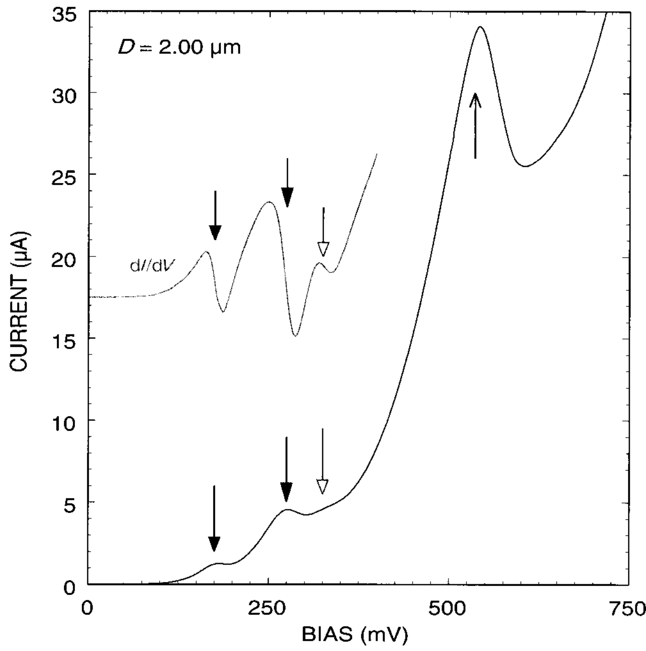

FIG. 2. $I(V)$ characteristics of a large $D=2.0\ \mu$m triple-barrier device at $T=1.7$ K, showing the peaks corresponding to resonant tunneling through the 2D subbands confined in the active region together with dI/dV data of the lower bias $I(V)$ peaks corresponding to tunneling through strongly coupled 2D subbands. The first two peaks at ~175 and ~275 mV marked by solid arrows correspond to tunneling through HH-HH coupled subbands, and the weak peak at ~325 mV marked by an open arrow to a HH-LH coupling. The high bias peak at $V\sim 500$ mV corresponds to tunneling through the uncoupled LH subband of the first well only.

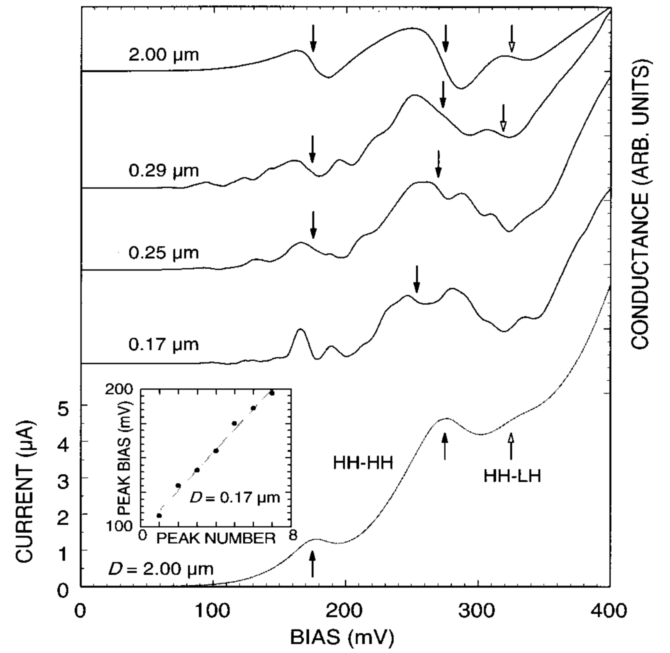

FIG. 3. Resonant tunneling current characteristics of $2.0 \geqslant D \geqslant 0.17\ \mu$m triple-barrier devices at $T=1.7$ K. The peaks corresponding to resonances through 2D subband levels are clear in the dI/dV data. The middle resonant peak shifts towards lower bias with decreasing mesa diameter, while the lowest bias peak stays roughly at the same bias. The highest bias peak shifts initially to lower bias; however, the fine structure which develops for $D \leqslant 0.29\ \mu$m renders the position of this peak unobtainable for $D \leqslant 0.25\ \mu$m. The solid arrows point to resonances through 2D HH-HH subbands, and the open arrow to HH-LH resonance. The fine structure is due to inhomogeneous-strain-induced lateral quantization of the 2D subbands confined in the active region and dominates the resonant tunneling data of the smallest devices. The graph in the inset plots the peak position of the quasiperiodic fine structure against the peak number of the $D=0.17\ \mu$m device. The solid line is a linear fit through the data points showing the uniform periodicity.

in Figs. 2 and 3 are at ~175, ~275, and ~325 mV. The first two strong peaks (marked with solid arrows) correspond to tunneling through HH-HH coupled subbands, and the weak peak (marked with open arrow) to a HH-LH coupling.[15] Because of the asymmetry of the triple-barrier RT structure, in reverse bias the HH subbands of the two quantum wells will not line up for a strong HH-HH coupling (see Fig. 1). Similarly, in reverse bias the HH-LH coupling becomes weak by the time the corresponding subband levels align with the Fermi sea in the emitter. Hence the $I(V)$ peaks in reverse bias correspond to tunneling through very weakly coupled subbands in individual wells, and will not be discussed in this paper.

In Fig. 3, we present the dI/dV data of $D=2.0$, 0.29, 0.25, and 0.17 μm devices where a shift in the main peak positions (marked with arrows) and a consistent development of a quasi-periodic fine structure in the RT data for $D \leqslant 0.29\ \mu$m is observable. The quasiperiod is ~12 mV, corresponding to ~3 meV of peak separation, for all sizes. The fine structure is reproducible upon temperature cycling.

We attribute the size-induced variations in the $I(V)$ characteristics to the changes in the 2D subband energies of the active region due to strain relaxation. These 2D subband energies depend on the individual subband energies in the neighboring quantum wells and the coupling among the subbands through the middle barrier—all sensitively affected by the strain in the $Si_{0.8}Ge_{0.2}$ wells and the Si middle barrier layers. The free surface of a mesa etched from a strained heterostructure allows the relaxation of the strained layers on the outer walls resulting in a nonuniform strain distribution especially strong at the perimeter, as displayed in the inset of Fig. 4. Figure 4 presents the radial component of the strain, ϵ_{rr}, on the midplanes of the two wells and the middle barriers of $D=0.30$, 0.25, 0.20, and 0.15 μm $Si/Si_{0.8}Ge_{0.2}$ triple-barrier structures as a function of in-plane radius $r_\perp$ calculated by finite-element simulations based on a linear elastic model[19] that was used previously to calculate the strain in submicron double-barrier structures.[12] In these calculations, strain is normalized to the magnitude of full biaxial strain. A negative value corresponds to biaxial compression of the lattice, and a positive one to biaxial expansion: in a $Si/Si_{0.8}Ge_{0.2}$ structure fully strained to the Si substrate the strain in the $Si_{0.8}Ge_{0.2}$ layers is $\epsilon_{rr}=-1$, and in the Si layers it is $\epsilon_{rr}=0$.

Figure 4 shows that the radial component of the strain in the $Si_{0.8}Ge_{0.2}$ layers decreases gradually with $r_\perp$ from the center of the pillar ($r_\perp=0$), with a strong inhomogeneous region of increasing strain near the surface ($r_\perp=D/2$). A ringlike region with $\epsilon_{rr}\approx 0.4$ and a radial extent of ~100 Å runs around the perimeter of the structure for all D. The strain in the two SiGe wells is very similar except at the

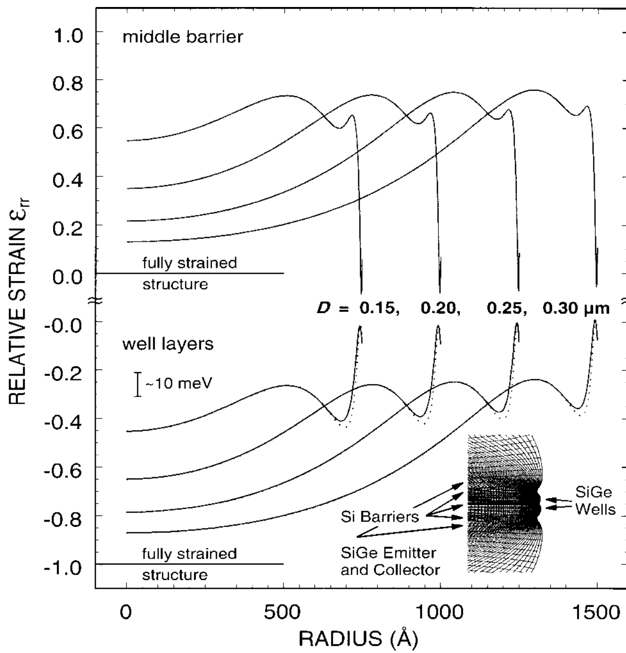

FIG. 4. Calculated relative radial extensional strain component ϵ_{rr} as a function of radius $r_\perp$ for $D=0.30$, 0.25, 0.20, and 0.15 μm $Si/Si_{0.8}Ge_{0.2}$ triple-barrier structures on the midplane of the $Si_{0.8}Ge_{0.2}$ wells (lower plots) and Si middle barrier (upper plots) layers. The Inset shows the magnified displacement of the finite element mesh corresponding to a section of the active region near the sidewall. The solid lines in the lower plots give the strain in the first well ($W_1=35$ Å), and the dotted lines in the second well ($W_2=28$ Å). The relative strain $\epsilon_{rr}=-1$ is normalized by system mismatch strain such that, in large, fully strained devices, in the strained $Si_{0.8}Ge_{0.2}$ layers it is $\epsilon_{rr}=-1$ and in the (unstrained) Si layers it is $\epsilon_{rr}=0$. The negative strain values correspond to biaxial compression and positive values to biaxial expansion of the in-plane lattice component. The expansion in Si middle barrier layers of the relaxed nanostructures induced by the relaxing $Si_{0.8}Ge_{0.2}$ wells is clearly observable in the upper plots.

perimeter where the strain is strongly nonuniform. In this region the relaxation is larger in the thicker well layer. In the thin (~10 Å) middle Si barrier sandwiched between the two well layers, the strain is positive because of the biaxial expansion of the barrier layer induced by the relaxation of the wells. The strain profile of the middle barrier follows the strain profile of the well layers very closely, except for the small deviation in the outer nonuniform region. The strain profiles indicate that the strain at the perimeter depends strongly on local relaxation, whereas the strain in the center region reflects collective relaxation of the whole heterostructure. Here we would also like to emphasize that the strain in the middle barrier affects the interwell coupling.

We calculate the resonant subband energies of the triple-barrier structures by the usual 6×6 Luttinger-Kohn Hamiltonian.[20,21] The effects of the bias-dependent interwell coupling are included by using self-consistent calculations of the potential distribution over the device, and assuming constant potential throughout each layer. Uniform strain relaxation is incorporated into the calculations by varying the strain energy term in the Luttinger-Kohn Hamiltonian.[2,4,20,21] To see the effects of uniform strain relaxation on the subband energies as a function of device diameter, we used the strain values at the centers of the wells for each D (Fig. 4). Previously, when we used the same method to calculate the subband energies in double-barrier structures with different diameters, the results were in good agreement with energy differences extracted directly from the RT data.[14]

In double-barrier structures, the shift in the lowest HH and LH 2D subband levels relative to the Fermi level in the emitter with applied bias is approximately equal to the change in the electrostatic potential in the center of the well independent of the details of the wave functions as long as the bias is not too large. In triple-barrier structures, the confined 2D subband energies are more sensitive to the applied bias because a change in bias shifts the subband levels in the neighboring wells relative to each other, affecting the coupling among them; therefore, energy differences between the 2D subbands of triple-barrier structures cannot be extracted reliably from the data using self-consistent calculations. Hence we have chosen to predict the resonant peak positions with the following simple approximation. In the sequential tunneling model,[16] the tunneling current is given by $I \propto N(V)T_e(V)$, where the supply function $N(V)$ is defined as the number of holes satisfying the E and $\mathbf{k}_\perp$ tunneling selection rules, and $T_e(V)$ is the transmission coefficient through the first barrier. $N(V)$ depends on the geometry of the dispersion, and $T_e(V)$ on the form of the wave-functions of the confined subband involved in the tunneling. Because of charge accumulation near the emitter barrier of the RT structure under bias (shown in the insets of Fig. 1), the peak current is expected to occur when the energy of the 2D subband falls below the Fermi level E_F, and is somewhat above the bulk valence-band edge in the emitter.[17] In triple-barrier structures, the coupled subbands are strongly nonparabolic, and the form of the wave functions is different for each subband. Therefore, we chose to use the $I(V)$ of the large $D=2.0\ \mu$m device as a reference to estimate the resonant peak positions of smaller devices.

Before we present our results, we feel it is important to describe the effects of strain relaxation on the confined subbands and the RT $I(V)$ characteristics of the triple-barrier structures. When in a strained SiGe layer the strain relaxes uniformly, HH-LH band-edge splitting reduces, and the band gap increases[2]—effectively increasing the energy of the holes in the valence band. It is well known (experimentally and theoretically) that in strained Si/SiGe heterojunctions, where SiGe layers are strained compressively to unstrained planar Si substrates, the conduction-band alignment is negligible and the valence-band offset is almost equal to the band gap. In SiGe/Si, where Si layers are under tensile strain, the band alignment is such that the band offset in the conduction band is larger than that of the valence band.[5] The band alignments in Si/SiGe heterostructures where both sides of the interface are under some strain have not been studied as thoroughly. In our calculations, we have assumed that in the ranges of strain we are interested in, the band-gap offset is mostly in the valence band. This assumption only affects the effective barrier heights, which do not have a strong influence on the subband energies; further, our previous calculations based on this assumption give excellent agreement with data of double-barrier structures.

The change in band gap due to strain relaxation is larger than the changes in the HH-LH splitting. Effectively, strain

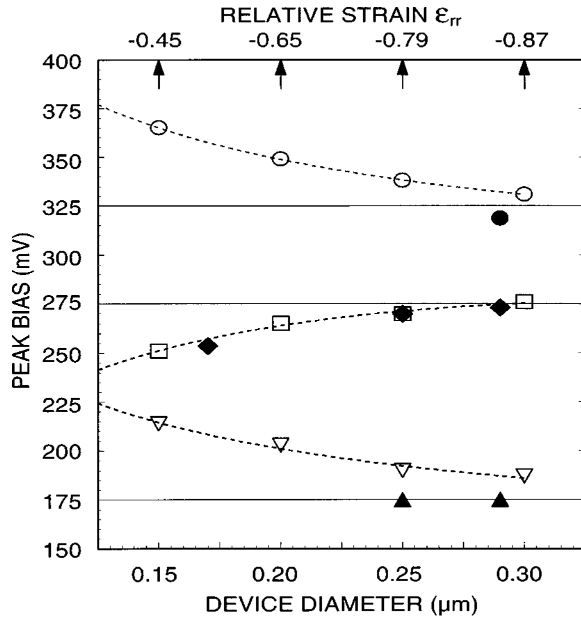

FIG. 5. Estimated resonant peak positions of the uniformly relaxed triple-barrier structures for $D=0.30$, 0.25, 0.20, and 0.15 μm triple-barrier resonant tunneling structures (open points) and the measured main peak positions as a function of device diameter for $D=2.0$, 0.29, 0.25, and 0.17 μm (solid points). The corresponding relative strain ϵ_{rr} values are shown on the upper (nonlinear) x axis marked with arrows. The horizontal lines mark the measured peak positions of the large structures ($D\geqslant 2.0\,\mu$m) with full biaxial strain. The dashed lines through the calculated points are quadratic fits to serve as guides to the eye.

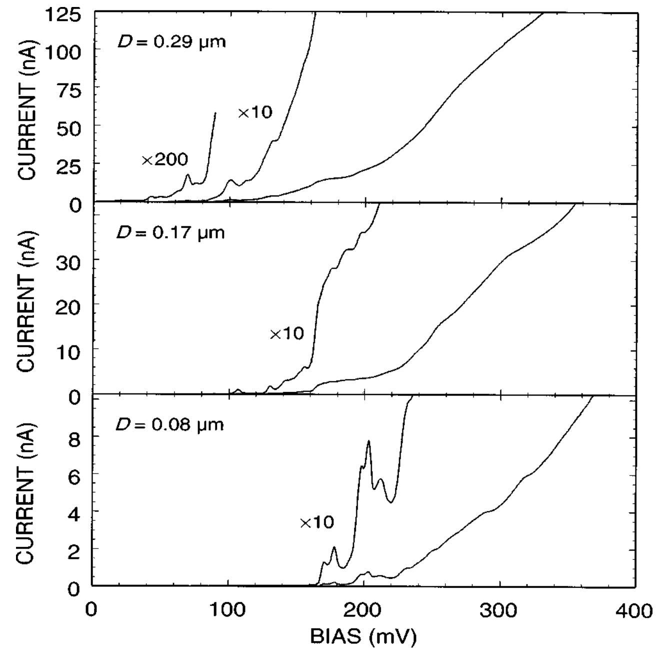

FIG. 6. Resonant tunneling $I(V)$ of $D=0.29$, 0.17, and 0.08 μm triple-barrier structures. The fine structure in the $I(V)$ is due to the quantization of the 2D subbands by the inhomogeneous-strain-induced lateral confinement potential. The increase in the onset of the current as D is decreased is partially due to an increase in the ground-state energy of laterally confined states and also due to different amounts of relaxation in the emitter region and the active region of the structure where the subbands are confined.

corresponds to lower potential for both heavy and light holes, allowing one to read the strain profiles of the SiGe well layers in Fig. 4 as (nonuniform) lateral confinement potential profiles. On the other hand, the strain in the Si barriers induced by the relaxation of the SiGe layers should also be considered. The strain in the middle barrier affects the coupling between the surrounding wells through the change in barrier height as well as the change in the interaction between the different hole bands. The heights of the barriers are determined by interpolating the strain-dependent valence-band offsets at the heterojunction.[5]

In submicron structures the strain relaxation in the emitter region is smaller than the strain relaxation in the active region of the structure surrounded by the two outer barriers because of the constraining effect of the thick outer Si regions. According to the affects of strain explained above, larger strain in the emitter regions translates to higher energies for the confined subbands, as measured from the Fermi level of the emitter region, shifting the RT $I(V)$ peaks to higher bias.

We have estimated effects of uniform strain relaxation on the $I(V)$ peak positions. In the calculations, we have used the strain at the center of each well (from Fig. 4) and an average of the strain values in the center of the emitter along the tunneling direction. Figure 5 summarizes our results (open points), and compares them to our data (solid points). The dashed lines in the figure going through the calculated (open) points are guides to the eye. The calculations are in very good agreement with data for the device sizes and the $I(V)$ peaks where the peak integrity is not destroyed by the fine structure. In the region where the fine structure washes out the main tunneling peaks, the calculations based on uniform strain assumption are not valid. Instead, the calculations should include the inhomogeneous-strain-induced lateral confinement potentials to estimate the corresponding quantization energies.

Figure 6 presents the development of fine structure in the RT $I(V)$ at $T=1.7$ K of $D=0.29$, 0.17, and 0.08 μm devices for $V\leqslant 400$ mV. In $D\leqslant 0.17\,\mu$m structures the fine structure in the tunneling current dominates the entire low-bias range. We attribute the fine structure in the $I(V)$ to inhomogeneous strain induced lateral quantization of the 2D subbands in the active region of the triple-barrier structure (similar to double-barrier devices[11,12]). The onset of the current increases by ~60 mV as D is decreased from ~0.29 to ~0.17 μm, and by ~120 mV when $D=0.08\,\mu$m. This increase is partially due to an increase in the ground-state energy of laterally confined states, and also due to different amounts of relaxation in the emitter region and the active region of the structure where the subbands are confined. A series resistance is ruled out as a source of the shift of the current onset to higher bias, because the corresponding higher-bias LH peaks with much higher peak currents (Fig. 2) do not show any effects of a series resistance. A more careful analysis of the fine structure in the $I(V)$ of $D\leqslant 0.2\,\mu$m structures and the inhomogeneous-strain-induced lateral confinement potentials will be published later. Here we find it sufficient to present the magnetotunneling $I(V,B_{\parallel})$ at $T=1.7$ K of the $D=0.17\,\mu$m device near the tunneling threshold in Fig. 7. As $B_{\parallel}$ is parallel to the tunneling direction, the $B_{\parallel}$-induced confinement is superimposed on the lateral inhomogeneous-

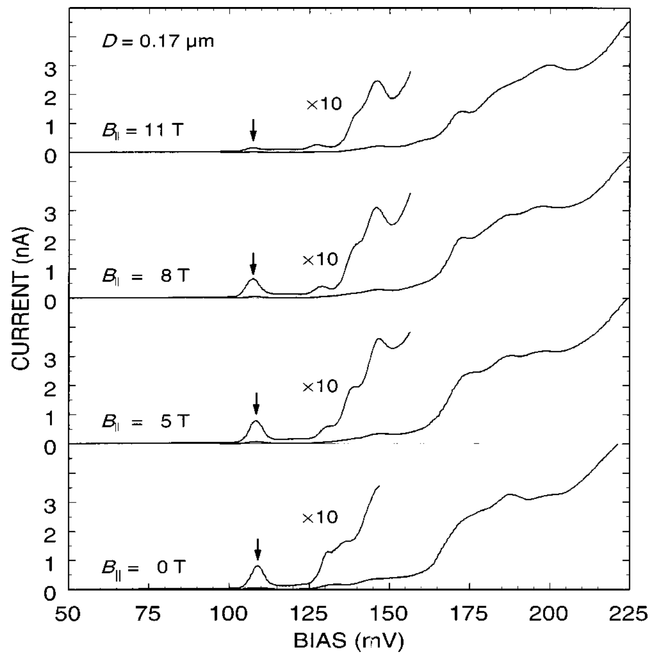

FIG. 7. Resonant tunneling data in external parallel ($\mathbf{B}_{\parallel}\|\mathbf{I}$) magnetic fields of the $D=0.17\ \mu$m triple-barrier resonant tunneling structure. The quenching of the fine structure in the onset of the tunneling current at $B_{\parallel}\sim 11$ T suggests an effective lateral potential length of $\sim$75 Å in the active region.

strain-induced potential. The fine structure in the onset of the tunneling current is quenched near $B_{\parallel}=11$ T. This implies that the strain-induced lateral potential length scale confining the holes is comparable to the $\sim$75 Å magnetic length at 11 T, which is in reasonable agreement with the calculated strain profiles of Fig. 4. The lateral extent of the ringlike region in the strain profile at the perimeter is $\sim$100 Å for all D. Further, the lateral length scale of the ground state of a hole with effective mass $m^{*}\sim 0.25m_e$ in the corresponding inhomogeneous-strain-induced harmonic potential of the $D=0.15\ \mu$m structure is $\sim$100 Å.

In conclusion, we have used resonant tunneling measurements to probe the effects of strain relaxation in individual p-Si/Si$_{0.8}$Ge$_{0.2}$ triple-barrier nanostructures with various diameters in the $2.0\leqslant D\leqslant 0.17\ \mu$m range. In the tunneling current we observed shifts in the resonant peaks due to changes in the strain-dependent energy levels of the coupled 2D resonant subbands. The observed fine structure in the $I(V)$ due to resonances through coupled inhomogeneous-strain-induced discrete hole states became stronger with decreasing lateral dimension and started to dominate the $I(V)$ line shape at $D=0.17\ \mu$m. We have employed Luttinger-Kohn-type calculations incorporating strain distributions determined by finite-element techniques and potential profiles by self-consistent calculations to correlate the changes in the $I(V)$ to strain relaxation. Our measurements prove tunneling to be a useful spectroscopic probe for strain phenomena in individual nanostructures, and point out the surprisingly large influence size-induced strain relaxation exerts on the electronic properties of nanostructures. Finally, we suggest that inhomogeneous strain distribution due to size-induced strain relaxation may be utilized to fabricate quantum structures.

A.Z. and C.D.A. were supported by the NSF (DMR-9702725), the ONR Young Investigator Program (N00014-95-1-0729), and the Sloan Foundation; while H.T.J. and L.B.F. acknowledge support by ONR (N00014-95-1-0239) and the MRSEC Program of the NSF (DMR-9632524). The fabrication facilities at Brown University are supported in part by MRSEC (DMR-9632524).

[1] R. People, J. C. Bean, D. V. Lang, A. M. Sergent, H. L. Störmer, and K. W. Wecht, Appl. Phys. Lett. **45**, 1231 (1984).

[2] R. People, Phys. Rev. B **32**, 1405 (1985).

[3] C. G. V. de Walle and R. M. Martin, Phys. Rev. B **34**, 5621 (1986).

[4] G. L. Bir and G. E. Pikus, *Symmetry and Strain-Induced Effects in Semiconductors* (Wiley, New York, 1974).

[5] R. People, IEEE J. Quantum Electron. **22**, 1696 (1986).

[6] K. Kash, B. P. V. der Gaag, D. D. Mahonney, A. S. Gozdz, L. T. Florez, J. P. Harbison, and M. D. Sturge, Phys. Rev. Lett. **67**, 1326 (1991).

[7] D. Gershoni, J. S. Weiner, S. N. Chu, G. A. Baraff, J. M. Vanderberg, L. N. Pfeiffer, K. West, R. A. Logan, and T. Tanbun-Ek, Phys. Rev. Lett. **65**, 1631 (1990).

[8] T. Arakawa, S. Tsukamato, Y. Nagamune, M. Nishioka, J. H. Lee, and Y. Arakawa, Jpn. J. Appl. Phys. **32**, L1377 (1993).

[9] A. Zaslavsky, K. R. Milkove, Y. H. Lee, B. Ferland, and T. O. Sedgwick, Appl. Phys. Lett. **67**, 3921 (1995).

[10] L. De Caro, L. Tapfer, and A. Giuffrida, Phys. Rev. B **54**, 10 575 (1996).

[11] P. W. Lukey, J. Caro, T. Zijlstra, E. van der Drift, and S. Radelaar, Phys. Rev. B **57**, 7132 (1998).

[12] C. D. Akyüz, A. Zaslavsky, L. B. Freund, D. A. Syphers, and T. O. Sedgwick, Appl. Phys. Lett. **72**, 1739 (1998).

[13] H. T. Johnson, L. B. Freund, C. D. Akyüz, and A. Zaslavsky, J. Appl. Phys. **84**, 3714 (1998).

[14] C. D. Akyüz, H. T. Johnson, A. Zaslavsky, L. B. Freund, and D. A. Syphers, in *Future Trends in Microelectronics: Off the Beaten Path*, edited by S. Luryi, J. M. Xu, and A. Zaslavsky (Wiley, New York, 1999).

[15] B. Ferland, C. D. Akyüz, A. Zaslavsky, and T. O. Sedgwick, Phys. Rev. B **53**, 994 (1996).

[16] S. Luryi, Appl. Phys. Lett. **47**, 490 (1985).

[17] V. J. Goldman, D. C. Tsui, and J. E. Cunningham, Phys. Rev. B **35**, 9387 (1987).

[18] A. Zaslavsky, D. A. Grützmacher, S. Y. Lin, T. P. Smith III, R. A. Kiehl, and T. O. Sedgwick, Phys. Rev. B **47**, 16036 (1993).

[19] These calculations were performed using the ABAQUS finite element code for structural mechanics analysis (Hibbitt, Karisson & Sorensen, Inc., Pawtucket, RI, 1997).

[20] J. M. Luttinger and W. Kohn, Phys. Rev. **97**, 869 (1955).

[21] G. Shuberth, G. Abstreiter, E. Gornik, F. Shäffler, and J. F. Luy, Phys. Rev. B **43**, 2280 (1991).